Supporting Material

X-ray Absorption Spectroscopy of Dinuclear Metallohydrolases

David L. Tierney[†*] and Gerhard Schenk[‡]

[†]Department of Chemistry and Biochemistry, Miami University, Oxford, OH 45056, U.S.A.

[‡]School of Chemistry and Molecular Biosciences, The University of Queensland, St. Lucia, QLD 4072, Australia.

[*]Correspondence: tiernedl@miamioh.edu

Data Reduction

In practice, the EXAFS can be separated into two independent components: a smoothly varying background and an oscillatory interference pattern whose magnitude decreases monotonically with increasing energy. The smooth background represents the absorption of the free atom, which is usually unavailable, and is, therefore, approximated by fitting a 2-3 region spline (of quadratic or cubic polynomials) to the data above the edge (**Fig. S1**). The oscillatory portion of the spectrum that remains is a direct result of the local structure experienced by the absorbing atom. The damping of the oscillations as the energy increases is a measure of the disorder in the local structure, both static (variations in distance) and dynamic (thermal motion). While the static disorder cannot be experimentally controlled, the dynamic disorder, which is dominant near room temperature, can be effectively eliminated at cryogenic temperatures. The use of low temperature has the added benefit of reducing the radiation damage to the sample from prolonged exposure to high intensity ionizing radiation.

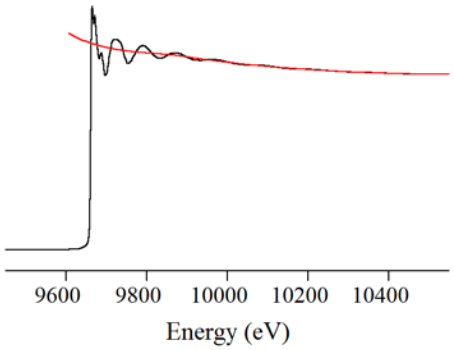

Fig. S1. Example of a spline background.

$$k = \frac{m_e v}{\hbar} = \frac{2\pi}{\lambda} = \left[\frac{2m_e}{\hbar^2}\left(E - E_0\right)\right]^{1/2} = \left[0.2625\left(E - E_0\right)\right]^{1/2} \qquad \text{(S1)}$$

Once isolated from the background, the EXAFS is typically subjected to Fourier analysis for frequency deconvolution. It is, therefore, useful to present the EXAFS as a function of the photoelectron momentum, or wave vector, *k*, (**Eq. S1**) which has units of inverse angstroms, $Å^{-1}$. This is analogous to photon momentum (wavenumber, cm^{-1}), except that, unlike a photon, the photoelectron has non-zero mass. Consequently, while

photon momentum is linearly dependent on its energy, photoelectron momentum is dependent on the square-root of its energy. **Eq. S1** holds for E expressed in electron volts (eV), where 1 eV = 1.6 x 10^{-19} J = 8066 cm^{-1}. In **Eq. S1**, m_e is the electron rest mass, h is Planck's constant and E_0 represents the energy required to promote an electron to the continuum (see **Fig. S1**). While E_0, which depends on the local structure of the metal ion, could, in principle, be experimentally obtained from X-ray photoemission spectroscopy (XPS), it is impractical to measure. Therefore, E_0 is either treated as a variable parameter in EXAFS analysis or held fixed at a calibrated value, obtained from analysis of a compound of known structure.

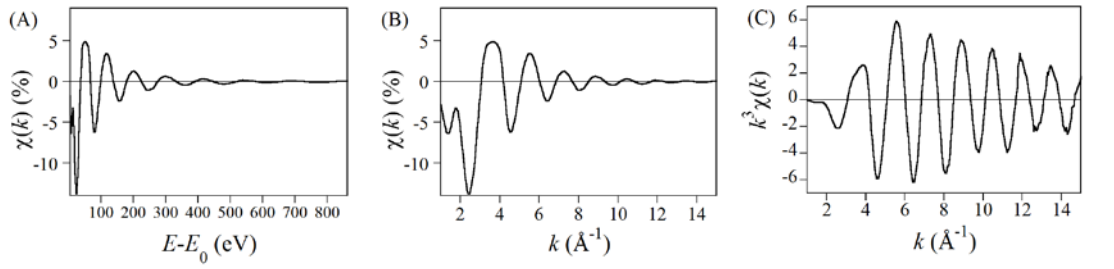

Fig. S2. Presentation of the background subtracted EXAFS for a ZnS_4 metal site (χ) (A) *vs.* energy above E_0, as a percentage of the atomic absorption (edge jump) (B) *vs. k* and (C) *vs. k*, weighted by k^3.

Care must be taken to keep the initial value of E_0 constant when comparing EXAFS datasets (typically 15-20 eV above E_0 for the elemental form of the metal of interest), as it is this initial value that sets the reference energy when the data are converted to *k*-space. Given the approximately k^3 decay of the EXAFS amplitude, it is common to display the raw EXAFS data weighted by k^3 to accentuate the oscillations at higher photoelectron momentum (**Fig. S2**). As is apparent in **Fig. S2**, the inherent signal-to-noise drops precipitously with increasing energy. Consequently, data integration times are also often scaled by k^3, so that the majority of the time invested in data collection is spent in the region where the signal intensity is lowest.

A Fourier transform (FT) takes the dependent variable into the inverse space of the independent variable. Therefore, an FT of the *k*-space EXAFS ($Å^{-1}$) has units of

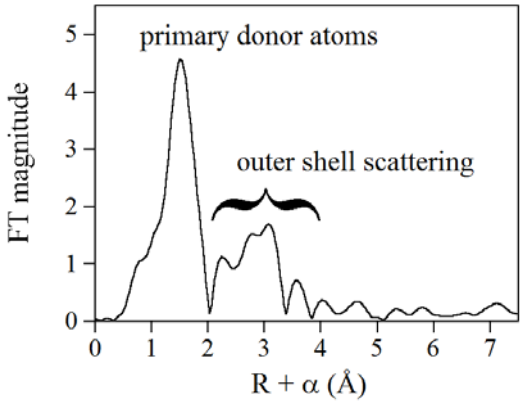

Fig. S3. EXAFS Fourier transform indicating the metal ion's primary coordination sphere and the outer shell scattering associated with rigidly held, distant atoms.

distance (Å). For randomly oriented samples, such as frozen solutions, the observed EXAFS is the sum of all possible orientations, and the FT represents a pseudo-radial distribution function (RDF) about the central atom. The peaks in the FT then represent a group of atoms at a similar distance (referred to as "shells," **Fig. S3**). It is not a true RDF because of the phase-shift (ϕ_{as}) experienced by the photoelectron as it passes through the atomic potentials (electron clouds) of the absorber and the scatterer (typically *ca.* -0.4 Å in *R*-space). In recent years, it has become common to present phase-shifted Fourier transforms, where the phase-shift is applied *prior* to Fourier transformation, effectively displaying the data on a "true" distance axis (*R*, rather than $R + \alpha$). However, this point deserves a word of caution. As different atoms with different atomic potentials will necessarily produce a different phase-shift, the phase-shift is unique to a given absorber-scatterer pair. Only one phase-shift can be applied to the data prior to Fourier transformation, making this is a dangerous practice for a heterogeneous metal site with mixed N/O/S donor sets, potentially obscuring minor contributors, such as the single sulfur donor in the dinuclear active site of class B1 metallo-β-lactamases (0.5 S per Zn, see text).

While the FT is useful for visualization of the data, it is the *k*-space data that are fit in determining the most consistent structural model. The use of Fourier filtering (forward transformation, Gaussian windowing and back-transformation into *k*-space) allows deconvolution of the observed EXAFS into its component frequencies (**Fig. S4A**) and can be used to remove high frequency noise (**Fig. S4B**). However, as with any Fourier transform, the reverse FT is sensitive to the endpoints chosen. In particular, when

frequencies differ by distances close to the resolution of the data (below), the two peaks overlap significantly in the FT and they may effectively cancel, leading to a false zero point. If this false zero is used as one of the window limits, real contributions can be unintentionally removed by the Fourier filter, leading to exclusion of a shell of scatterers that is actually present. An example of this is shown below. It is, therefore, critical that any analysis be carried out on both filtered and unfiltered data to ensure the consistency of the model.

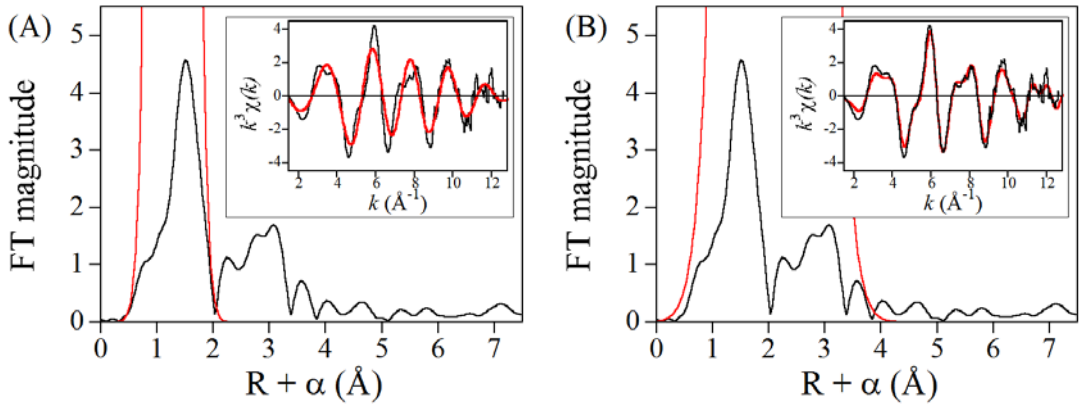

Fig. S4. Application of a Gaussian window and Fourier filtering (A) to isolate a particular shell or (B) to remove high frequency noise.

EXAFS Data Fitting

Most EXAFS analysis software starts from the plane-wave approximation, which assumes the inter-atomic distance is large relative to the photoelectron momentum, allowing its description as a planar wave propagating with uniform velocity along the vector that connects the absorbing and scattering atoms. Above $k \sim 1$ Å^{-1}, this assumption is valid. The curved-wave approximation takes the angular variation of propagation into account, allowing extension of the data analysis below $k = 1$ (92). The most simplistic interpretation of EXAFS is the single-scattering (SS) formalism (93, 94). This approach assumes that the only phenomena observed are two-body, single-scattering events. The advantage of the SS formalism is its simplicity. However, this approach neglects

scattering pathways involving three or more atoms and thus ignores any angular information that may be contained in the EXAFS. Recent theoretical advances have made multiple scattering calculations more straightforward, allowing inclusion of scattering events involving 3 or more atoms in the analysis (95-102).

$$\chi(k) = \sum \frac{N_{as} A_s(k) S_c}{kR_{as}^{\ 2}} \exp(-2k^2 \sigma_{as}^{\ 2}) \exp(-2R_{as}/\lambda) \sin[2kR_{as} + \phi_{as}(k)] \qquad \text{(S2)}$$

$$R = \frac{\sum_{i=1}^{N} \left(\chi_{i,obs} - \chi_{i,calc}\right)^2}{\sum_{i=1}^{N} \left(\chi_{i,obs}\right)^2} \qquad \text{(S3)}$$

The EXAFS can be described, to first order, by **Eq. S2**. Structural information is extracted from the EXAFS *via* a least-squares fit to **Eq. S2**. The quality of the fit is judged by the magnitude of some form of fit residual, such as that given in **Eq. S3**, where a smaller residual indicates smaller deviation between the model and the data (*i. e.*, a better model). In **Eq. S2**, N_{as} represents the number of like atoms at a given distance from the absorber (the number of atoms in a shell); S_c is the scale factor, which is specific to the absorber-scatterer (*as*) pair and largely independent of energy; $A_s(k)$ represents the backscattering power of the scattering atom; R_{as} is the average absorber-scatterer interatomic distance. The sum is taken over all shells of scatterers. The first exponential damping term, exp ($-2k^2\sigma_{as}^{\ 2}$), where σ_{as} is the rms variation in R_{as} (assuming thermal disorder is negligible), is known as the Debye-Waller factor. The second damping term, exp ($-2R_{as}/\lambda$), where λ is the mean free path of the photoelectron, accounts for losses in amplitude due to inelastic scattering of the photoelectron. These first three terms in **Eq. S2** derive from evaluation of the first moment of the EXAFS and define the observed amplitude. The amplitude effectively represents the probability of photoelectron scattering, which depends on both the identity of the scattering atom (larger atoms = larger probability) and the number of scattering atoms. The combination of similarity in

size and similar phase shifts affected by atoms within the same period makes it difficult to distinguish scattering atoms within Z ~ 8 (such as N and O), but relatively easy to distinguish scatterers from different rows of the periodic table (such as N/O and S). This point is illustrated in **Fig. S5** for zinc-nitrogen and zinc-sulfur scattering, which are out of phase over most of the *k*-range that is common to EXAFS studies of metalloproteins.

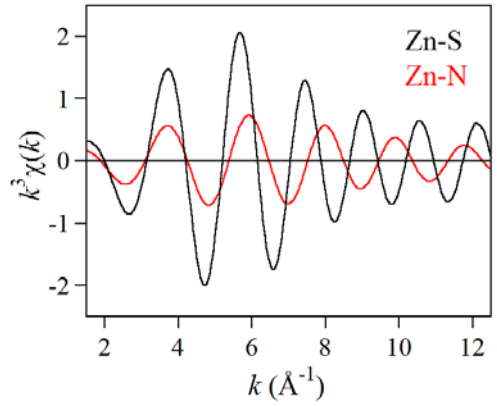

Fig. S5. Relative phases of Zn-N (2.00 Å) and Zn-S (2.30 Å) scattering.

The final term in **Eq. S2**, $\sin[2kR_{as} + \phi_{as}(k)]$, comes from evaluation of the second moment of the EXAFS, and defines the frequency of the oscillations. Its linear dependence on the absorber-scatterer distance illustrates how the frequency of the EXAFS provides direct information on distance. Short distances produce low-frequency oscillations, while longer distances lead to higher frequency oscillations. Also included in the argument of the sine function is $\phi_{as}(k)$, the aforementioned phase-shift experienced by the photoelectron as it passes through the atomic potentials of the absorbing and scattering atoms. In order to extract structural information from the EXAFS, it is necessary to provide the amplitude ($A_s(k)\exp(-2R_{as}/\lambda)$) and phase ($\phi_{as}(k)$) functions for each absorber-scatterer pair. These functions may be obtained either empirically, from the measured EXAFS of a structurally characterized small molecule, or, as is more common, by one of several theoretical calculations (96, 103, 104).

Use of theoretical amplitude and phase functions to fit data from an unknown structure requires that the scale factor (S_c) and the shift in E_0 (ΔE_0) be calibrated by fitting EXAFS data for crystallographically characterized small molecules, in order to minimize the number of variable parameters in fitting the unknown data (discussed

further below). In general, fits to model data will refine S_c, ΔE_0, σ_{as} and $R_{as,}$ while holding the coordination number fixed at the crystallographically determined value. Provided this fit gives the correct bond length with a reasonable value of σ_{as}, the refined values of S_c and ΔE_0 can then be used, and held fixed, in fits to the EXAFS data for unknown systems. It is important to realize that S_c is an absorber-scatterer dependent parameter. Each type of scattering interaction will have a different optimal value. In contrast, E_0 (and, therefore, ΔE_0) is defined by the metal ion. Consequently, while there is still some debate on this issue, it is largely accepted that a single value of ΔE_0 should be used for all shells included in a fit. Caution should be used when refining ΔE_0, as this is equivalent to refining the phase-shift in the course of the fit.

Limitations

There are, essentially, three observables in an EXAFS spectrum: amplitude, frequency and phase. From the amplitude of the observed EXAFS, the scatterer identity, coordination number and relative disorder can be determined. However, these parameters are highly correlated. For example, if the data are fit with a coordination number that is higher than the true coordination number, σ_{as} will refine to an unreasonably large value to reduce the apparent amplitude. In practice, the EXAFS coordination number is determined with an accuracy of *ca.* 25%, or ± 1, although the precision is significantly better.

In contrast to the amplitude, the frequency of the EXAFS, and thus the distance obtained, is very well determined. The absorber-scatterer distance is usually accurate to ± 0.02 Å, with a precision of ± 0.005 Å. As such, the average bond length derived from a least-squares fit to the first shell is a strong indicator of the metal ion's primary coordination number. Comparison of average metal-ligand bond lengths from small molecule crystal structures shows that, in general, an increase of ~ 0.1 Å can be anticipated for each additional ligand. For example, a survey of the Cambridge

Crystallographic Database shows average bond lengths of 1.95, 2.07 and 2.18 Å for 4-, 5- and 6-coordinate Zn(II), respectively, with all nitrogen donors. These values will shorten slightly for every nitrogen donor that is replaced with an oxygen donor, and lengthen for every nitrogen donor that is replaced with a sulfur donor.

$$\Delta R = \frac{\pi}{2\Delta k} \qquad N_{idp} = \frac{2\Delta R \Delta k}{\pi} \tag{S4}$$

As with any least-squares procedure, a good fit can always be obtained with a sufficient number of variable parameters. The corollary to that statement is that a *better* fit will always be obtained with *more* variable parameters. It is, therefore, important to understand the limitations of the information content of an EXAFS spectrum. The inherent distance resolution of a set of EXAFS data is inversely proportional to the span of the data in *k*-space ($\Delta k = k_{max}$-k_{min}, **Eq. S4**). Inspection of **Eq. S4** shows that in order to distinguish two shells separated by 0.10 Å, the *k*-range of the data must be at least 15.7 Å^{-1}. Typically, EXAFS spectra for a biological sample will span Δk ~ 10-12 Å^{-1}, carrying 0.16 – 0.13 Å resolution. Thus, a multi-component fit that refines to distances that differ by less than this value cannot be considered a valid model.

Eq. S4 also defines the number of independent points, N_{idp}, in an EXAFS dataset, which is an indication of the number of variable parameters that can be refined with confidence. For a single shell of scatterers, ΔR will be on the order of 1.2 Å, giving a total of *ca.* 8 independent points for Δk = 10 Å^{-1}. This value is larger than the five parameters that can be varied for a single shell (ΔE_0, S_c, N_{as}, R_{as} and σ_{as}), and in refining all five, the variables will be slightly over-determined. However, addition of a second type of scatterers would double the number of variables, and the fit would then be under-determined. Thus, it is important to carefully control, or at least be cognizant of, the number of variable parameters used to fit the data. The most common approach to controlling the number of refined variables is to hold ΔE_0 and S_c fixed at calibrated

values, obtained as described above, refining R_{as} and σ_{as}, and stepping N_{as} through all reasonable integer or half-integer values, using the fit residual to define the best-fit coordination number.

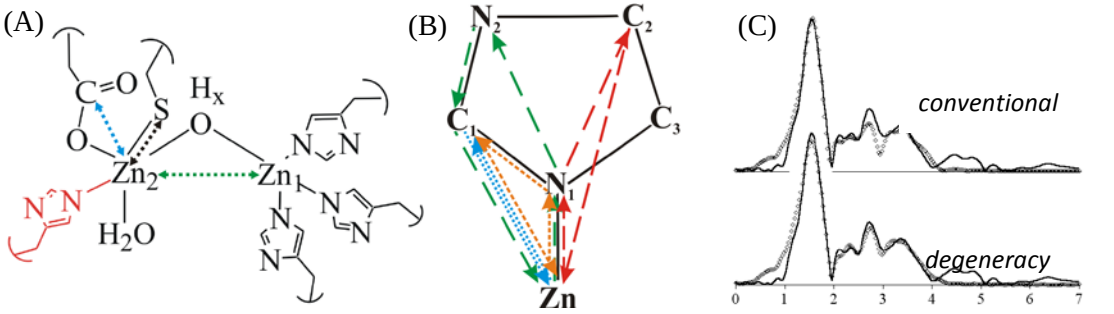

Fig. S6. (A) Active site of a B1 M
to its EXAFS data. (B) Subset of the multiple scattering pathways available with a coordinated imidazole. (C) Comparison of fits to $[Zn(Im)_4]^{2+}$ EXAFS data using conventional method and degeneracy-based method.

Deconvolution of a complex metal site

It is useful to define a strategy for fitting the data from a complex metal site. As much of the mini-review deals with EXAFS data of metallo-β-lactamases (MβLs), we will outline the strategy in use in our laboratories, in the context of a class B1 MβL, which has two Zn(II) ions in its active site. One of the Zn(II) ions is coordinated by three histidine side chains and a water molecule that bridges the two metals. The second Zn(II) is coordinated by one of every biologically relevant ligand: a monodentate carboxylate (asp), one histidine, one cysteine, a terminal water molecule and the bridging solvent (**Fig. S6**). The *average* Zn(II) coordination sphere consists of 4 N/O and 0.5 S donors in the primary coordination sphere, with two histidine side chains, a Zn-Zn interaction and possibly a carboxylate carbon contributing to the outer shell scattering (**Fig. S3**). As EXAFS is a bulk measurement, it is this average environment that will be detected. The approach outlined below is certainly not the only one that has been employed, nor is it the

only one that is valid. We developed this protocol purely with an eye on being conservative in our interpretation of the data.

The most difficult aspects of EXAFS analysis of a metal site such as this are reliable identification of the Zn-S scattering and extraction of the Zn-Zn interatomic distance in the presence of a relatively large background of imidazole outer shell scattering. Identification of the sulfur donor is complicated by its low occupation (1 out of 9 ligands) and the presence of the carboxylate carbon atom which resides at a similar distance (~ 2.5 Å relative to ~ 2.3 Å for the Zn-S). These interactions can effectively cancel each other when the carboxylate is held in a well-ordered configuration, as these two interactions will be out of phase with each other. The net result is that the apparent contribution of the Zn-S scattering path is reduced as the two distances converge, as illustrated in **Fig. S7**.

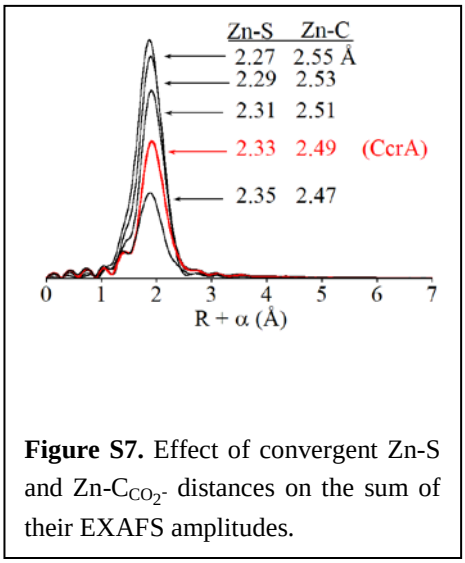

Figure S7. Effect of convergent Zn-S and Zn-C_{CO_2}- distances on the sum of their EXAFS amplitudes.

Multiple scattering interactions from within the rigid ring system of a coordinated imidazole are well known in metalloprotein EXAFS, producing four features of near equal intensity in the FT (see **Fig. S6**), and a number of approaches to their quantification have been put forth. In principle, the observed scattering pattern contains both distance and angular information, although the angular information is difficult to extract, especially when more than one such ligand is present. A full multiple-scattering calculation of a simple metal-imidazole interaction, such as that shown in **Fig. S6**, will identify 140 distinct scattering paths, 35 of which are predicted to display intensities of 10% or greater relative to the metal-nitrogen single-scattering pathway. The most historically common approach to fitting imidazole outer shell scattering fits the four most prominent scattering pathways to the data, allowing R_{as} and σ_{as} for each to refine,

holding their coordination numbers fixed at the degeneracy of the path, as defined by the calculation. The disadvantage of this approach is that it neglects 21 of the 35 paths that produce significant scattering intensity. Newer software packages allow the linking of multiple pathways, affording the opportunity to fix the imidazole ring as a rigid unit, refining all of the distances in a correlated fashion. This, however, enforces idealized bond angles on the metal-histidine interaction that may not be representative of the real arrangement.

We have taken a more pragmatic approach to this problem. If one accepts that there is angular variability, and that this cannot be easily predicted, then it is better to refine all of the metal-histidine associated paths independent of one another. Given that the degeneracy of the most prominent paths only account for 14 of the 35 paths with significant scattering power, we chose to include them indirectly by grouping them by distance relative to the four most prominent. We then replace the degeneracy of the individual paths with the sum degeneracy of paths of similar length. In our hands, this approach produces a better fit to all four outer shell features (see **Fig. S6C**), which is critical to extraction of the metal-metal scattering in these systems, with one single atom bridge and separations of *ca.* 3.4 Å.

The process we follow is straightforward, as outlined in **Fig. S8**. Starting with the Fourier-filtered first shell (**Fig. S4A**), we first fit it with low-Z (N/O) scatterers and determine their best fit coordination number, in half-integer steps, determined by that which produces the smallest fit residual (**Eq. S3**). We then add S scatterers, also in half-integer steps, monitoring the improvement in the fit residual, with fits that produces less than ~ 50 % improvement considered unjustified. Once the best first shell fit has been obtained, we return to the full spectrum (**Fig. S4B**), fitting the Fourier-filtered data for the sake of comparing smaller fit residuals. Using the full span of the data, we add in imidazoles, again in half-integer steps, reporting that which produces the smallest fit residual. We estimate the uncertainty in the number of imidazole scatterers determined in

this way to be ± 0.5. It is at this point that we add in the metal-metal scattering pathway, again looking for a significant reduction in fit residual. Using this procedure, improvements of 40 – 70 % are attainable for well-ordered systems. Generally, fits that produce smaller improvements are not interpreted as indicative of metal-metal scattering, and the metal-metal path is not reported. For each step in fitting the full dataset (with and without inclusion of metal-metal scattering), we compare the basic N/O/S + imidazole (± metal-metal) fit to one that includes a metal-carbon shell, to assess the potential effect of the carboxylate carbon on the overall model. Again, we stress here that all Fourier-filtered fits are compared to fits to the as-isolated *k*-space data, to ensure the reliability of the fit.

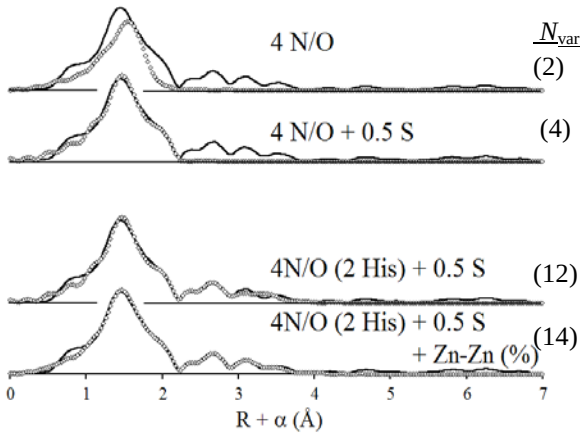

Fig. S8. Stepwise process of building up a structural model consistent with the EXAFS of an MβL.

Experimental considerations.

The general setup of an XAS experiment is shown in **Fig. S9**. The experiment involves stepping through the incident X-ray energy while measuring incident (I_0) and transmitted (or fluorescent) X-ray intensity (I_1 or FF). X-ray intensity is measured using gas-filled ionization chambers (I_0, I_1 and I_2) that consist of a large surface area capacitor whose plates are parallel to the direction of light propagation. The X-ray beam passing between the plates ionizes the gas

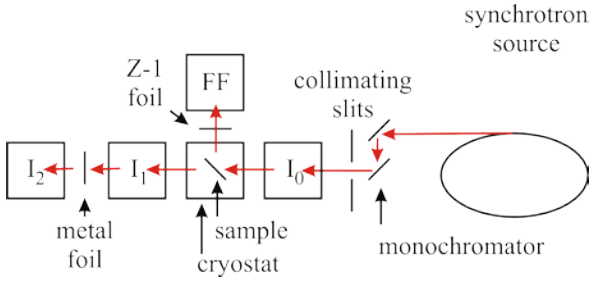

Figure S9. Schematic of an XAS experimental setup.

in the chamber, allowing current flow between them, proportional to the photon density per unit time. Monochromatic radiation is typically obtained by using an in-line double crystal monochromator, taking advantage of Bragg reflection ($n\lambda = 2d\sin\theta$) from specific crystal planes. The double crystal design allows the monochromatic radiation to exit the monochromator parallel to the incident radiation, maintaining constant beam position relative to the experimental setup, independent of the energy selected. To ensure accurate calibration of the energy, the XAS spectrum of a metal foil (positioned between I_1 and I_2 in **Fig. S9**) is measured at the same time as the experimental spectrum. The first inflection point of the spectrum from the elemental form of a metal occurs at a well-defined energy, and it is this point that is used to calibrate the experimental spectrum.

$$\Delta E = E(\Delta\theta)\cot\theta \qquad \text{(S5)}$$

The energy resolution is dependent on a number of factors. For a conventional flat crystal monochromator, the energy resolution is given by **Eq. S5**. In **Eq. S5**, θ is the Bragg angle at energy E, while $\Delta\theta$ is the spread in θ, which is defined by the vertical collimation of the X-ray source and the vertical divergence of the synchrotron source. Thus, the energy resolution is affected by the vertical size of the incident beam (*i. e.*, larger vertical size = lower energy resolution), which is defined by the collimating slits in **Fig. S9**. The breadth of the rocking curve (range of θ), and therefore the energy resolution, of a given crystal set is inversely proportional to the *d*-spacing of that crystal. Thus, better energy resolution is obtained with Si(220) crystals, with a *d*-spacing of 1.92 Å, than with Si(111) crystals, with a *d*-spacing of 3.14 Å.

By definition, Bragg reflection contains contributions from higher order harmonics ($n > 1$), in addition to the fundamental frequency. For example, a Si(220) monochromator set to deliver 9 keV photons will also pass 18 keV photons. Therefore, the experimental setup must include some method of harmonic rejection. The two most common methods of harmonic discrimination are “de-tuning” the monochromator and

use of an in-line mirror (between the monochromator and the collimating slits in **Fig. S9**). The former takes advantage of the narrower rocking curve for reflection of the harmonic compared to the fundamental, reducing the harmonic content of the reflected radiation by rotating one of the crystals in a double crystal setup slightly off parallel. The disadvantage of this simple approach is that it simultaneously reduces the incident intensity of *both* the fundamental and the harmonic, reducing the amount of the desired signal that is detected. The in-line mirror allows use of the full intensity of the incident X-ray beam. The angle of the mirror relative to the incident x-ray beam allows external reflection of the fundamental frequency, while higher harmonics are absorbed *via* total internal reflection.

XAS spectra of may be collected as transmission ($\ln(I_0/I_1)$ *vs. E*) or flourescence excitation spectra (FF/I_0 *vs. E*, using a fluorescence detector oriented normal to the incident X-ray beam), depending on the concentration of the analyte. For concentrations of *ca.* 20 mM or higher, the transmission experiment will afford better results. For metalloproteins, where concentrations are often limited to ~ 1 mM, K_α fluorescence excitation spectra offer greater sensitivity, particularly with the development of energy-discriminating solid-state detectors (the number of K_α photons emitted by the sample is directly proportional to the number of photons absorbed). However, fluorescence detection is typically limited in the number of photons that can be counted per unit time. As the fluorescence detector will see both fluorescent photons and elastically scattered photons (the strength of the solid state detector is the ability to distinguish them), the total incident count rate limits the photon density that can be employed. Contributions from the elastic scatter can be decreased by use of a low pass filter, typically the *Z*-1 metal foil placed in front of the fluorescence detector (*e. g.*, a Cu foil filter is used for measurement of Zn XAS).

Finally, it should be noted that any XAS experiment is only as good as the samples employed. Two key points should always be kept in mind. First, the reader is

reminded that XAS is a macroscopic technique that samples *all* populations of a given element in a sample. Therefore, it is critical that *all* of the metal of interest in a sample resides in a homogeneous environment. Any adventitiously bound metal will contribute to the measured EXAFS, giving a weighted average of all of the structures that are present. Second, the reader is reminded that diffraction occurs in all directions. The presence of ice crystals in a sample can effectively destroy an XAS experiment, as diffraction is much stronger than fluorescence, introducing artifacts into the spectrum that may, or may not, be obvious. For this reason, it is desirable to include a glassing agent, such as glycerol, to prevent formation of ice crystals on freezing.

REFERENCES

92. Mustre de Leon, J., J. J. Rehr, S. I. Zabinsky, and R. C. Albers. 1991. *Ab initio* Curved-Wave X-Ray-Absorption Fine Structure. *Phys. Rev. B* 44:4146-4156.
93. Ashley, C. A. and S. Doniach. 1975. Theory of extended x-ray absorption edge fine tructure (EXAFS) in crystalline solids. *Phys. Rev. B* 11:1279-1288.
94. Stern, E. A., D. E. Sayers, and F. W. Lytle. 1975. Extended x-ray-absorption fine-structure technique. III. Determination of physical parameters. *Phys. Rev. B* 11:4836-4846.
95. O'Day, P. A., J. J. Rehr, S. I. Zabinsky, and G. E. Brown, Jr. 1994. Extended X-Ray Absorption Fine Structure (EXAFS) Analysis of Disorder and Multiple-Scattering in Complex Crystalline Solids. *J. Am. Chem. Soc.* 116:2938-2949.
96. Ankudinov, A. L., B. Ravel, J. J. Rehr, and S. D. Conradson. 1998. Real Space Multiple Scattering Calculation and Interpretaton of XANES. *Phys. Rev. B* 58:7565-7576.
97. Rehr, J. J. and A. L. Ankudinov. 2005. Progress in the theory and interpretation of XANES. *Coord. Chem. Rev.* 249:131-140.
98. Ankudinov, A. L. and J. J. Rehr. 2003. Development of XAFS Theory. *J. Synchrotron Rad.* 10:366-368.
99. Ankudinov, A. L. and J. J. Rehr. 2000. Theory of Solid State Contributions to the X-Ray Elastic Scattering Amplitude. *Phys. Rev. B* 62:2437-2445.
100. Poiarkova, A. V. and J. J. Rehr. 1999. Multiple-Scattering X-ray-Absoption Fine-Structure Debye-Waller Factor Calculations. *Phys. Rev. B* 59:948-957.
101. Rehr, J. J., R. C. Albers, and S. I. Zabinsky. 1992. High-Order Multiple-Scattering Calculations of X-Ray-Absorption Fine Strucutre. *Phys. Rev. Lett.* 69:3397-3400.
102. Rehr, J. J., J. Mustre de Leon, S. I. Zabinsky, and R. C. Albers. 1991. Theoretical X-Ray Absorption Fine Structure Standards. *J. Am. Chem. Soc.* 113:5135-5140.
103. Teo, B. K. and P. A. Lee. 1979. *J. Am. Chem. Soc.* 101:2815-2832.
104. Gurnman, S. J., N. Binsted, and I. Ross. 1984. *J. Phys. C: Solid State Phys.* 17:143-151.